



RESEARCH ARTICLE

10.1002/2016JE005010

Key Points:

- Raman spectra of glasses are presented for a large range of chemical compositions, analogous to Martian compositions
- Spectral intensities are parameterized to derive a model for estimation of the glass composition from Raman spectra
- This enables in situ estimations of glass compositions in extraterrestrial or submarine volcanic settings

Supporting Information:

- Table S1
- Supporting Information S1
- Data Set S1
- Data Set S2

Correspondence to:

D. Di Genova,
danilo.digenova@min.uni-muenchen.de

Citation:

Di Genova, D., S. Kolzenburg, A. Vona, M. O. Chevrel, K.-U. Hess, D. R. Neuville, W. Ertel-Ingrisch, C. Romano, and D. B. Dingwell (2016), Raman spectra of Martian glass analogues: A tool to approximate their chemical composition, *J. Geophys. Res. Planets*, 121, doi:10.1002/2016JE005010.

Received 2 FEB 2016

Accepted 18 APR 2016

Accepted article online 20 APR 2016

©2016. The Authors.

This is an open access article under the terms of the Creative Commons Attribution-NonCommercial-NoDerivs License, which permits use and distribution in any medium, provided the original work is properly cited, the use is non-commercial and no modifications or adaptations are made.

Raman spectra of Martian glass analogues: A tool to approximate their chemical composition

Danilo Di Genova¹, Stephan Kolzenburg², Alessandro Vona³, Magdalena Oryaëlle Chevrel⁴, Kai-Uwe Hess¹, Daniel R. Neuville⁵, Werner Ertel-Ingrisch¹, Claudia Romano³, and Donald B. Dingwell¹

¹Department of Earth and Environmental Sciences, Ludwig-Maximilians-Universität, Munich, Germany, ²Dipartimento di Scienze della Terra, Università degli Studi di Torino, Turin, Italy, ³Dipartimento di Scienze, Università degli Studi Roma Tre, Rome, Italy, ⁴Laboratoire Magmas et Volcans, Université Blaise Pascal, Aubière, France, ⁵Géomatériaux, CNRS-IPGP UMR 7154, Paris Sorbonne Cité, Paris, France

Abstract Raman spectrometers will form a key component of the analytical suite of future planetary rovers intended to investigate geological processes on Mars. In order to expand the applicability of these spectrometers and use them as analytical tools for the investigation of silicate glasses, a database correlating Raman spectra to glass composition is crucial. Here we investigate the effect of the chemical composition of reduced silicate glasses on their Raman spectra. A range of compositions was generated in a diffusion experiment between two distinct, iron-rich end-members (a basalt and a peralkaline rhyolite), which are representative of the anticipated compositions of Martian rocks. Our results show that for silica-poor (depolymerized) compositions the band intensity increases dramatically in the regions between 550–780 cm^{-1} and 820–980 cm^{-1} . On the other hand, Raman spectra regions between 250–550 cm^{-1} and 1000–1250 cm^{-1} are well developed in silica-rich (highly polymerized) systems. Further, spectral intensity increases at $\sim 965 \text{ cm}^{-1}$ related to the high iron content of these glasses ($\sim 7\text{--}17 \text{ wt } \% \text{ of } \text{FeO}_{\text{tot}}$). Based on the acquired Raman spectra and an ideal mixing equation between the two end-members we present an empirical parameterization that enables the estimation of the chemical compositions of silicate glasses within this range. The model is validated using external samples for which chemical composition and Raman spectra were characterized independently. Applications of this model range from microanalysis of dry and hydrous silicate glasses (e.g., melt inclusions) to in situ field investigations and studies under extreme conditions such as extraterrestrial (i.e., Mars) and submarine volcanic environments.

1. Introduction

Advanced imaging spectroscopy and instrument technologies have established Raman spectrometry as a powerful technique for rapid and precise determination of the distribution of assorted compounds in heterogeneous samples. Both inorganic and organic materials can be identified in situ with a submillimeter resolution, under extreme conditions and with little to no sample preparation (see Tarcea *et al.* [2008] and Greenberger *et al.* [2015] for reviews).

Due to their intrinsic analytical capabilities, Raman spectrometers have been developed for two forthcoming Mars missions (ExoMars program (2016–2018) and Mars 2020). They form a key component in the suite of analytical instrumentation for the planetary rovers, which are intended to both investigate geological processes and search for evidence of biological activity on Mars.

The design of these planetary rovers is dependent on (1) preliminary instrument testing for which the identification of appropriate analogue samples is required [e.g., Mustard *et al.*, 2013; Hutchinson *et al.*, 2014; Motamedi *et al.*, 2015] and (2) the availability of a database of Raman spectra capable both of chemical and mineralogical identification.

Recently, Raman spectroscopy has been successfully employed in the identification of minerals (hosted in rocks), which may be considered as analogue materials of Mars (i.e., Marion Island [Prinsloo *et al.*, 2011] and Icelandic tephra [Bathgate *et al.*, 2015]). These studies also reported features in their Raman spectra, which clearly could be interpreted as glassy silicate phases.

Moreover, Raman spectroscopy has also been developed as a tool to investigate volcanic (calc-alkaline) glasses and approximate their chemical composition [Di Genova *et al.*, 2015], to estimate the iron oxidation state of iron-rich basaltic glasses and alkali- and silica-rich glasses [Di Genova *et al.*, 2016], as well as to

determine the presence of water in silicate glasses [e.g., Thomas, 2000; Zajacz et al., 2005; Behrens et al., 2006; Le Losq et al., 2012].

Iron-rich basalts are widely dispersed on the Martian surface (see McSween [2015] for a review). Further, several recent studies [e.g., Christensen et al., 2005; Horgan and Bell, 2012; Blake et al., 2013; Vaniman et al., 2013; Bish et al., 2013; Downs, 2015; Grotzinger et al., 2015; Kah, 2015; Newsom et al., 2015; Cannon and Mustard, 2015] observed high abundances of alkali- and silica-rich amorphous materials in sedimentary rocks and impact-related deposits on the Martian surface and in Martian meteorites. In particular, Horgan and Bell [2012] observed large glass dune fields, which may testify to the existence of extensive explosive volcanism, possibly due to magma-water interaction, and where glass grains are presumably altered by water. Yet the characteristics of glass composition and origin are poorly constrained. Further, the recent study from Cannon and Mustard [2015] proposes that impactite (glassy material resulting from impact) found on Mars could “provide a means to trap signs of ancient life.” Thus, although glass seems to be a common feature on Mars and a key to understanding both Martian magmatic and surface processes, no precise compositional data exists as of yet.

Here we expand the compositionally dependent Raman database recently presented [Di Genova et al., 2015, 2016] to iron-rich basaltic and rhyolitic melts relevant to Mars. Those papers have shown how the presence of iron, and its oxidation state, greatly affects the Raman spectral features of glasses. This is evident, for example, when comparing the rhyolitic (sample Y12, iron-poor) end-member spectrum reported in Di Genova et al. [2015] with the iron-rich rhyolite spectrum showed in Di Genova et al. [2016] (sample Fsp1). As discussed in detail in Di Genova et al. [2016], the presence (or absence) of the band located at $\sim 970\text{ cm}^{-1}$ is the most direct spectral signature that enables identification of a glass as iron-rich (or iron-poor). This band is the expression of the Fe^{3+} in fourfold coordination in the glass structure. Through this spectral element, the iron oxidation state may be estimated by Raman spectroscopy. These considerations have brought us to the conclusion that the model to estimate the chemical composition of iron-poor glasses (typical from calc-alkaline volcanic system of our planet) presented in Di Genova et al. [2015], where the 970 cm^{-1} band is absent, is not suitable for Mars where iron-rich samples are expected. Therefore, a new model calibrated on iron-rich glasses is required.

We performed a diffusion experiment between iron-rich basaltic and rhyolitic melts considered as analogues for materials identified on the surface of Mars. The diffusion experiment produced a wide range of intermediate compositions between the two end-members. We systematically acquired Raman spectra across the diffusion interface and correlated these spectra to the local chemical composition.

Assuming a linear mixing model for the evolution of the acquired spectra, we retrieve a Raman parameter, which is then employed to estimate the chemical composition of glassy samples. The linear assumption has been validated in previous studies [Di Genova et al., 2015, 2016] as enabling the extraction of quantitative information from Raman spectra. Here we confirm that a more complex parameterization of the spectra is not required. This calibration broadens the compositional range of application of our previously published Raman model to include spectra of alkali and iron-rich glasses, which correspond to the chemical range anticipated on Mars.

With the benefit of this calibration, Raman spectroscopic investigation should now allow for a rapid, remotely controlled and in situ identification and investigation of silicate glasses as expected for future extraterrestrial rover missions (e.g., Mars).

2. Experimental Methods

2.1. Starting Material

The starting materials for the experimental syntheses consisted of anhydrous and bubble-free glasses of (1) synthetic iron-rich basalt and (2) natural peralkaline iron-rich rhyolite (pantellerite) equilibrated under reducing conditions. The first material consists of an iron-rich ($\sim 20\text{ wt } \% \text{ FeO}_{\text{tot}}$) basaltic composition exemplifying the known variety of Martian basalts [Chevrel et al., 2014]. Its composition was calculated from equilibrium melting of a primitive mantle composition (given by Dreibus and Wanke [1984] for a pressure of 13 kbar and a Martian mantle temperature of 1400°C , corresponding to 15% of mantle partial melting [Baratoux et al., 2011]). This sample is hereafter defined as “basaltic end-member” and named HDM according

to *Chevrel et al.* [2014]. The second sample was collected from Punta Spadillo, Pantelleria Island, Italy (see *Di Genova et al.* [2013] for sample location). It has a silica-, alkali- and iron-rich composition, hereafter defined as “rhyolitic end-member” and named PS. The natural rock was powdered and melted in air at 1500°C. The melt was homogenized by continuous stirring in a concentric cylinder apparatus at atmospheric conditions for 24 h and quenched afterwards.

Considering the reduced state of Martian conditions [e.g., *McSween et al.*, 1996; *Ghosal et al.*, 1998; *Herd et al.*, 2002; *Righter et al.*, 2008] and in order to avoid iron-oxide crystallization due to the high iron content of the samples, both the basaltic and rhyolitic end-members were equilibrated under reducing conditions. For this, each sample was placed in a vertical gas-mixing furnace equipped with a gas tight alumina muffle tube and CO-CO₂ gas mixing lines. The oxygen fugacity $f(\text{O}_2)$ was controlled by the CO-CO₂ gas mixtures and monitored by an yttrium-stabilized, zirconia-based oxygen sensor. The samples were kept at 1400°C and under $-10 \log f\text{O}_2$ for at least 24 h in order to ensure equilibrium. The reduced melts were then rapidly quenched to avoid oxidation (see *Chevrel et al.* [2014] and *Di Genova et al.* [2016] for details).

Optical and electron microscopy investigation proved that the obtained glasses were free of bubbles and crystals. Their redox state was measured on approximately 25 mg of material by a wet-chemistry method based on the potentiometric titration of potassium dichromate (see *Chevrel et al.* [2014] for details). The rest of the material was used for the diffusion experiment.

2.2. Diffusion Experiments Under Reduced Conditions

The diffusion experiment was performed in an Al₂O₃ crucible under reduced conditions. The basaltic end-member was first melted into the ceramic crucible (~5 min), and the rhyolitic end-member was then loaded above. This allows a gravitationally stable melt interface as a result of the density contrast between the melts (2376 kg m⁻³ for PS sample and 2767 kg m⁻³ for HDM, after *Lange and Carmichael* [1990] at the experimental T of 1400°C).

The diffusion experiment was performed at 1400°C for a duration of 4 h under the same oxygen fugacity as used in the synthesis ($-10 \log f\text{O}_2$). At the end of the experiment, rapid quenching was achieved by immersing the base of the crucible in distilled water. A polished section, perpendicular to the contact surface between the two end-members, was exposed in order to perform chemical and Raman spectroscopic analyses along the maximum chemical gradient.

2.3. Chemical Analysis

The major element composition along the diffusion interface was determined at the Department of Earth and Environmental Sciences at the University of Munich, using a Cameca SX100 electron microprobe analyzer (EMPA) with 15 kV acceleration voltage and 5 nA beam current. In order to reduce the alkali volatilization the beam diameter was defocused down to 10 μm. Both the employed standards and the applied matrix correction are reported in *Di Genova et al.* [2015]. The accuracy was better than 2.5% for all analyzed elements.

2.4. Raman Spectroscopy

Two different micro-Raman spectrometers, calibrated using a silicon standard, were employed to acquire Raman spectra; (1) HORIBA LabRAM HR at the Dipartimento di Scienze at the Università degli Studi di Roma Tre to collect spectra along the glassy filament and (2) HORIBA XploRA ONE at the Department of Earth and Environmental Sciences at the University of Munich to collect the external samples spectra. The micro-Raman spectrometers are equipped with a green argon ion laser (532 nm) focused through a 100× objective. Optical filters were employed in order to achieve ~2.5 mW at the surface of the glassy interface. The Raman systems were set with 600 T and 1200 T gratings, exposure time 90 s (3 times), confocal hole of 200–500 μm, and slit of 200 μm, and the spatial resolution of the sample surface is ~1 μm (theoretical spatial resolution = $0.61 \lambda/\text{NA}$ where λ is the wavelength of the laser (532 nm), and NA is the numerical aperture of the microscope objective being used (0.9 for 100×)).

Raman spectra were acquired over the range from 50 to 1500 cm⁻¹. A correction for the wavelength of the laser and temperature dependence of the spectra intensity was applied to all the acquired spectra according to *Shuker and Cammon* [1970] and *Long* [1977] approaches. Later, a baseline correction has been applied to all the spectra according to the strategy reported in *Di Genova et al.* [2015]. Finally, spectra were normalized in order to obtain an intensity maximum of 100 auxiliary units.

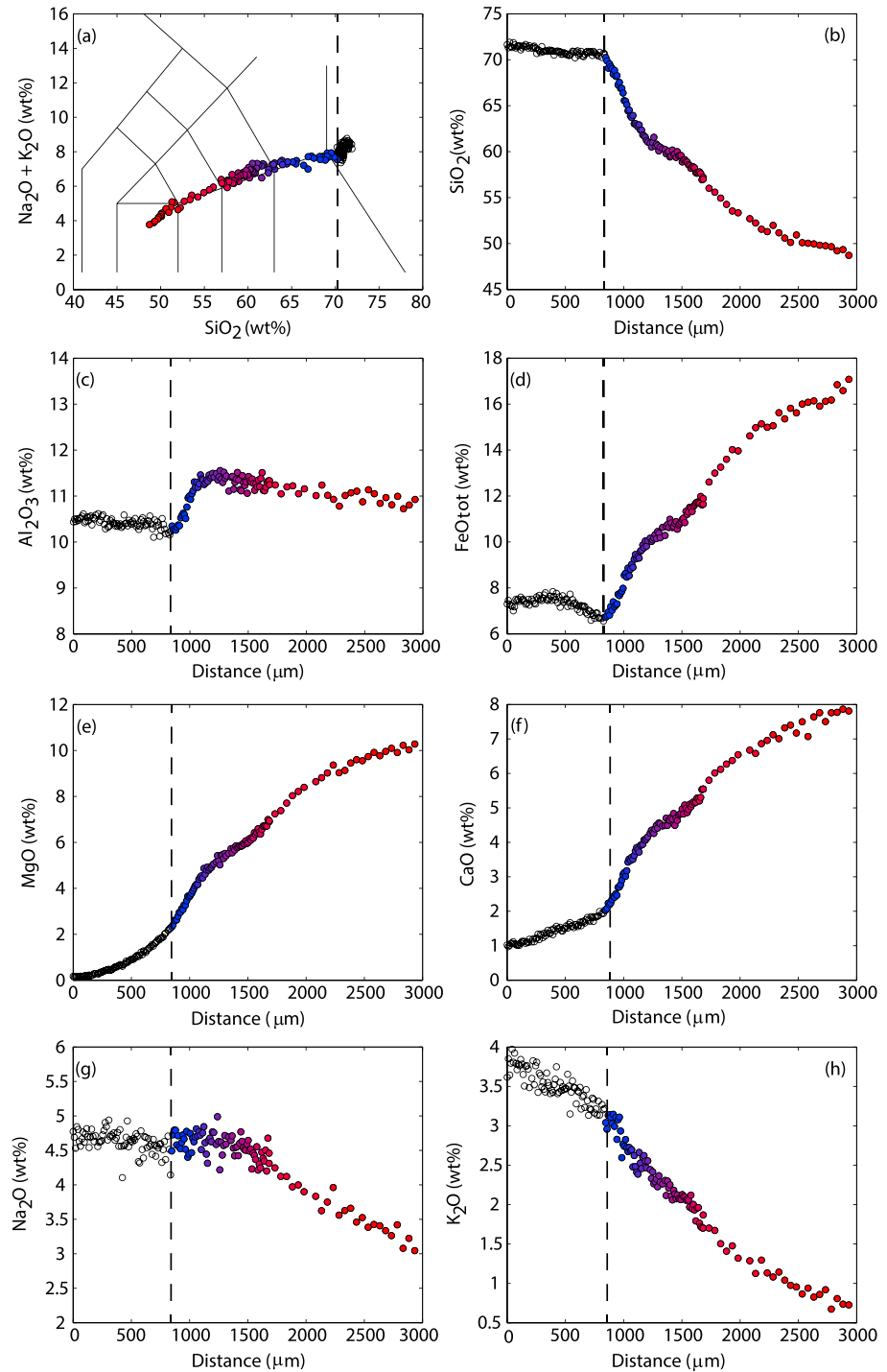


Figure 1. (a) TAS (total alkali versus SiO_2 contents in wt %) diagram showing the chemical composition of glasses used in this study; (b–h) measured chemical composition as a function of the distance along the analyzed glassy filament. The color scale (from red to blue) codifies the evolution of the chemical composition, along the investigated glassy filament. As the composition of the glass becomes more rhyolitic the symbol color becomes more blue. White symbols represent the chemical composition of glasses excluded to develop the model (see text).

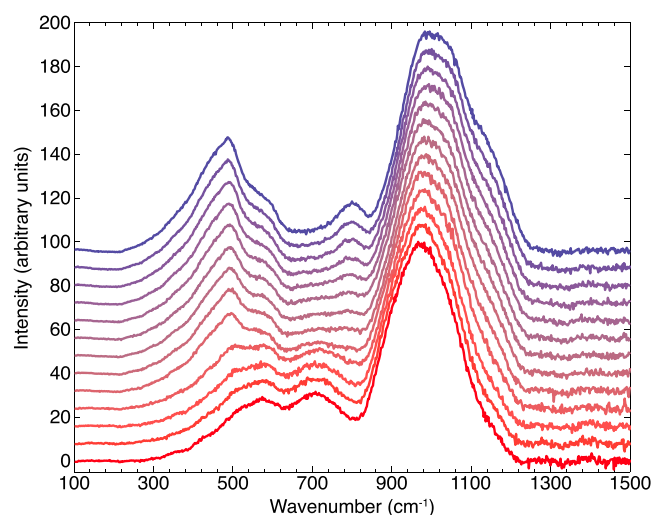


Figure 2. Long-corrected normalized acquired Raman spectra along the glassy filament. Symbol color scale codifies the evolution of chemical composition of the investigated glasses (see Figure 1). For better visualization, the spectra were offset vertically.

~47 and ~11 wt %, respectively; Na₂O, K₂O, CaO and MgO contents are ~2, ~0.1, 8 and 12 wt %, respectively. The Fe³⁺/Fe_{tot} is 0.45.

3.2. Chemical Compositions of the Diffusion Experiment

Examination of the experimental product by backscattered electron imaging and the lack of sharp peaks in the Raman spectra verify that the quenched material is glassy, thus preserving the compositions generated during the diffusion experiment.

The diffusive contact exhibits chemical boundary patterns spanning the entire range of compositions between both end-members. The chemical analysis result is reported in Table S1 in the supporting information and Figure 1 on a total alkali-silica (TAS) diagram and as a function of distance from the Si-rich (rhyolitic) to the Si-poor (basaltic) end-member, respectively. The length of the investigated profile, obtained from the experiment, is approximately 3000 μm.

The chemical composition varies continuously across the profile. Starting from the rhyolitic end-member we observe downhill diffusion [Chakraborty *et al.*, 1995] across the interface (~845 μm). This process is most prominent for iron, resulting in a decreasing FeO content down to ~6.9 wt %, which is lower than either end member composition. The silica content of the sample does not change strongly over this distance, and we therefore consider the composition with lowest Fe content (~845 μm) as the rhyolitic “end-member” of the mixing model.

3.3. Raman Spectroscopy

Figure 2 shows a selection of the Raman spectra acquired from the rhyolitic to basaltic end-members (in Figure S1 in the supporting information all the acquired Raman spectra are reported).

The Raman spectra can be divided into three main regions: the low-wave-number region (LW~250–650 cm⁻¹), the mid-wave-number region (MW~650–850 cm⁻¹) and the high-wave-number region (HW~850–1250 cm⁻¹).

The LW region is commonly ascribed to vibrations of bridging oxygens associated with three-, four-, five-, six-, or higher-membered rings of tetrahedra which participate in silicate networks [e.g., Bell *et al.*, 1968; Mysen *et al.*, 1980; McMillan *et al.*, 1982; Seifert *et al.*, 1982; Neuville and Mysen, 1996].

The structural contribution to the MW region is less constrained. The 800 cm⁻¹ band has been attributed, for pure silica glass, to Si-O stretching involving oxygen motions in the Si-O-Si plane [McMillan *et al.*, 1994] or to the motion of the Si in its oxygen cage [Mysen *et al.*, 1982]. The intensity of this peak decreases with increasing the network modifier content [Neuville *et al.*, 2014].

The HW region is related to stretching vibrations of T-O⁻ bonds associated to nonbridging oxygens (where T refers to fourfold coordinated cations (Si⁴⁺, Al⁴⁺, Fe³⁺), and it reflects the structural effects of the network-modifying or

3. Results

3.1. Chemical Compositions and Iron Oxidation State of the Starting Materials

The PS rhyolitic end-member [Di Genova *et al.*, 2013] is peralkaline with a calculated alpaicitic index of ~1.2. Measured main oxide content is ~72 and ~11 wt % for SiO₂ and Al₂O₃, respectively; iron (FeO) is ~7 wt %; Na₂O, K₂O, MgO and CaO contents are ~5, ~4, ~0.1 and ~1, respectively. The measured Fe³⁺/Fe_{tot}, determined by wet chemistry, is 0.37.

The HDM basaltic end-member [Chevrel *et al.*, 2014] is highly enriched in FeO (~19 wt %) and has SiO₂ and Al₂O₃ contents of ~47 and ~11 wt %, respectively; Na₂O, K₂O, CaO and MgO contents are ~2, ~0.1, 8 and 12 wt %, respectively.

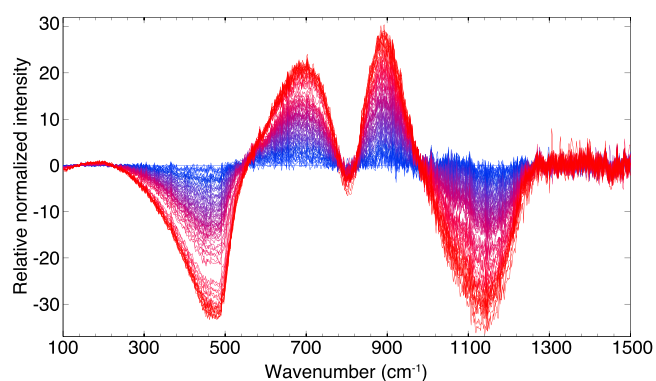


Figure 3. Evolution of the Raman spectra normalized to the rhyolitic end-member (blue). As the composition of the glass becomes more basaltic, the spectrum color becomes more red. The highly polymerized Si-rich glasses exhibit strong contributions in the spectral regions between 250–550 cm^{-1} and 1000–1250 cm^{-1} . Whereas the Raman spectra show an intensity increase in the regions between 550–780 cm^{-1} and 820–980 cm^{-1} associated with depolymerized Si-poor compositions.

at $\sim 400 \text{ cm}^{-1}$. In general, the intensity of the low-wave-number region for the basaltic composition (most depolymerized) is much lower than for rhyolitic, most polymerized, composition.

The MW region exhibits a symmetrical, broadband around $\sim 700 \text{ cm}^{-1}$ in the basaltic end member that shifts and sharpens to $\sim 800 \text{ cm}^{-1}$ in the rhyolitic end member (Figure 2).

In the HW region, the rhyolitic end-member spectrum displays an asymmetric band located between 850 and 1250 cm^{-1} . The spectrum shows a peak at $\sim 990 \text{ cm}^{-1}$ and two shoulders at ~ 1040 and $\sim 1150 \text{ cm}^{-1}$. In contrast, with decreasing SiO_2 content, the high-wave-number region exhibits a band occurring between 800 and 1200 cm^{-1} with a peak at around $\sim 965 \text{ cm}^{-1}$ and two shoulders located at $\sim 890 \text{ cm}^{-1}$ and $\sim 1040 \text{ cm}^{-1}$, respectively.

These features for LW, MW, and HW regions are in accordance with the results presented in *Di Genova et al.* [2016] for reduced pantelleritic glasses.

From these observations (Figure 2) we infer that both peak position and intensity of Raman spectra are intimately related to the changes in the glass structure (e.g., modification of inter-tetrahedral bond angles, force constants, T-O distances, and polymerization degree of the silicate structure) occurring in the samples with the variation of the chemical composition (see *Rossano and Mysen* [2012] and *Neuvill et al.* [2014] for reviews) and oxygen fugacity conditions [*Di Genova et al.*, 2016].

Figure 3 sums up the evolution of the acquired Raman spectra normalized to the rhyolitic end-member (blue), whereby a quantitative visualization of the change of the spectra with chemical composition is possible. The most significant intensity decreasing occurs in the regions between (1) 250 cm^{-1} and 550 cm^{-1} as well as (2) 1000 cm^{-1} and 1250 cm^{-1} , as these regions are clearly well developed in highly polymerized Si-rich systems (see *Neuvill et al.* [2014] for a review). Whereas the intensity increase occurs in the regions between (3) 550 cm^{-1} and 780 cm^{-1} , (4) 820 cm^{-1} and 980 cm^{-1} , associated with depolymerized Si-poor compositions (see *Neuvill et al.* [2014] for a review).

4. Discussion

4.1. From the Raman Spectra to the Chemical Composition of Iron-Rich Silicate Glasses: An Empirical Model

In order to estimate the chemical composition of the investigated samples we adopt the model reported in *Di Genova et al.* [2015] to empirically parameterize the recovered Raman spectra.

For this purpose, we combined the measured chemical composition with the collected Raman spectra (Table 1 and Figure S1) using an ideal mixing model (equation (1)). The Raman spectra were parameterized with

charge balancing cations [e.g., *Bell and Dean*, 1972; *Furukawa et al.*, 1981; *McMillan*, 1984; *Mysen*, 1988; *Neuvill et al.*, 2014]).

In the LW region, the rhyolitic end-member (blue color, Figure 2) shows a broad (asymmetric) band located at $\sim 489 \text{ cm}^{-1}$, a weak shoulder at $\sim 350 \text{ cm}^{-1}$ and another shoulder of higher intensity located at $\sim 580 \text{ cm}^{-1}$. With decreasing silica content (i.e., moving toward the basaltic end-member, red color, Figure 2), the LW Raman spectra change drastically in both peak position and intensity, showing a wider peak at $\sim 565 \text{ cm}^{-1}$, a shoulder at $\sim 590 \text{ cm}^{-1}$, and a weak shoulder

Table 1. Summary of Raman Parameters (R_p) Calculated Using Equation (1) and Chemical Composition (wt %) Along the Diffusive Contact

R_p	SiO ₂	TiO ₂	Al ₂ O ₃	FeO	MnO	MgO	CaO	Na ₂ O	K ₂ O	P ₂ O ₅	Tot
0.000	70.29	0.41	10.34	6.73	0.14	2.32	2.04	4.41	3.08	0.02	99.78
0.011	69.66	0.49	10.27	6.84	0.16	2.45	2.12	4.75	2.99	0.09	99.81
0.026	69.24	0.42	10.33	7.19	0.10	2.65	2.24	4.58	3.10	0.01	99.85
0.029	69.42	0.41	10.29	7.06	0.08	2.61	2.20	4.64	3.13	0.02	99.86
0.029	69.17	0.41	10.36	7.09	0.15	2.71	2.29	4.65	3.04	0.01	99.88
0.029	68.67	0.42	10.35	7.20	0.16	2.88	2.40	4.66	3.10	0.06	99.89
0.032	69.03	0.40	10.37	7.02	0.18	2.79	2.34	4.71	3.03	0.03	99.89
0.059	68.61	0.40	10.42	7.34	0.10	2.95	2.41	4.51	3.08	0.06	99.89
0.066	68.84	0.36	10.52	7.19	0.09	2.96	2.40	4.52	3.00	0.03	99.91
0.068	68.64	0.36	10.56	7.17	0.10	3.03	2.45	4.55	3.04	0.02	99.92
0.069	69.10	0.48	10.28	6.92	0.17	2.62	2.24	4.81	3.15	0.09	99.86
0.074	68.26	0.38	10.58	7.23	0.12	3.11	2.50	4.60	3.11	0.02	99.91
0.083	68.21	0.38	10.59	7.25	0.13	3.10	2.49	4.66	3.02	0.02	99.87
0.087	68.32	0.37	10.62	7.26	0.14	3.07	2.46	4.71	2.86	0.02	99.82
0.094	68.03	0.39	10.63	7.41	0.14	3.12	2.51	4.73	2.85	0.01	99.82
0.112	67.24	0.45	10.57	7.75	0.13	3.29	2.72	4.61	3.12	0.03	99.90
0.113	67.45	0.43	10.62	7.64	0.14	3.23	2.64	4.71	3.00	0.00	99.86
0.128	67.45	0.45	10.51	7.70	0.10	3.27	2.71	4.52	3.13	0.07	99.91
0.135	67.49	0.42	10.53	7.67	0.09	3.28	2.71	4.55	3.10	0.07	99.91
0.144	67.15	0.38	10.65	7.72	0.11	3.36	2.74	4.72	3.03	0.03	99.89
0.155	66.85	0.36	10.79	7.79	0.13	3.48	2.79	4.76	2.89	0.01	99.87
0.163	66.84	0.37	10.90	7.84	0.15	3.60	2.85	4.59	2.70	0.04	99.86
0.175	66.87	0.39	10.96	7.86	0.14	3.66	2.92	4.39	2.59	0.08	99.86
0.184	66.71	0.40	11.00	7.87	0.10	3.65	2.99	4.34	2.66	0.11	99.85
0.197	66.38	0.40	11.00	7.98	0.07	3.63	3.06	4.44	2.77	0.12	99.85
0.201	65.93	0.40	10.95	8.24	0.07	3.64	3.12	4.63	2.77	0.10	99.86
0.209	65.57	0.39	10.93	8.52	0.09	3.68	3.12	4.75	2.74	0.09	99.88
0.222	65.46	0.37	10.97	8.67	0.10	3.72	3.07	4.64	2.77	0.11	99.89
0.229	65.48	0.36	11.04	8.66	0.12	3.77	3.02	4.48	2.82	0.14	99.88
0.239	65.43	0.39	11.07	8.54	0.12	3.82	3.04	4.50	2.81	0.16	99.88
0.252	65.23	0.43	11.09	8.45	0.13	3.87	3.13	4.64	2.75	0.16	99.88
0.260	64.87	0.41	11.18	8.59	0.12	3.92	3.26	4.69	2.69	0.12	99.86
0.268	64.52	0.36	11.29	8.82	0.11	3.98	3.38	4.65	2.67	0.08	99.84
0.280	64.43	0.35	11.29	8.82	0.09	4.03	3.47	4.62	2.69	0.06	99.85
0.287	64.53	0.40	11.21	8.62	0.08	4.08	3.51	4.65	2.72	0.07	99.87
0.293	64.46	0.43	11.20	8.53	0.10	4.13	3.51	4.73	2.72	0.09	99.88
0.303	64.12	0.44	11.27	8.67	0.13	4.17	3.48	4.80	2.69	0.11	99.87
0.309	63.80	0.43	11.30	8.87	0.15	4.17	3.48	4.81	2.69	0.14	99.83
0.320	63.66	0.42	11.24	9.00	0.16	4.15	3.53	4.75	2.72	0.16	99.79
0.322	63.74	0.40	11.18	9.02	0.16	4.18	3.56	4.71	2.68	0.17	99.79
0.331	63.94	0.36	11.19	8.93	0.15	4.28	3.53	4.73	2.56	0.16	99.83
0.344	63.93	0.35	11.27	8.90	0.14	4.39	3.51	4.77	2.48	0.14	99.87
0.356	63.51	0.40	11.38	9.03	0.12	4.44	3.54	4.78	2.54	0.13	99.87
0.357	63.06	0.44	11.46	9.23	0.12	4.47	3.61	4.73	2.62	0.13	99.86
0.373	62.96	0.43	11.44	9.40	0.14	4.53	3.68	4.60	2.59	0.13	99.89
0.380	63.05	0.41	11.36	9.39	0.19	4.47	3.80	4.57	2.44	0.17	99.84
0.382	63.05	0.40	11.38	9.46	0.17	4.55	3.74	4.51	2.49	0.14	99.90
0.395	62.93	0.43	11.36	9.30	0.18	4.43	3.84	4.71	2.42	0.18	99.78
0.398	62.78	0.46	11.32	9.30	0.15	4.59	3.84	4.83	2.38	0.15	99.79
0.405	62.79	0.43	11.24	9.34	0.12	4.84	3.75	4.79	2.46	0.12	99.88
0.405	62.70	0.46	11.27	9.36	0.11	4.82	3.81	4.86	2.36	0.11	99.85
0.411	62.92	0.38	11.27	9.29	0.16	4.67	3.71	4.67	2.61	0.18	99.87
0.414	62.83	0.36	11.31	9.35	0.18	4.60	3.75	4.57	2.67	0.23	99.84
0.424	62.52	0.39	11.34	9.51	0.17	4.71	3.85	4.50	2.60	0.25	99.83
0.426	62.32	0.43	11.34	9.62	0.16	4.84	3.93	4.41	2.50	0.24	99.80
0.436	62.35	0.48	11.32	9.63	0.16	4.92	3.94	4.32	2.45	0.22	99.77
0.457	61.80	0.44	11.46	9.87	0.13	4.79	3.95	4.66	2.61	0.19	99.89
0.462	61.71	0.40	11.43	9.79	0.12	4.81	4.02	4.71	2.63	0.26	99.88
0.474	61.66	0.37	11.39	9.90	0.10	4.89	4.07	4.63	2.60	0.26	99.87
0.479	61.04	0.49	11.50	9.92	0.18	5.03	4.12	4.79	2.49	0.31	99.89
0.500	61.94	0.51	11.18	9.55	0.08	5.02	4.22	4.60	2.53	0.21	99.85

Table 1. (continued)

R_p	SiO ₂	TiO ₂	Al ₂ O ₃	FeO	MnO	MgO	CaO	Na ₂ O	K ₂ O	P ₂ O ₅	Tot
0.503	61.38	0.51	11.31	9.88	0.06	5.05	4.18	4.70	2.56	0.22	99.86
0.507	61.92	0.50	11.23	9.59	0.14	5.02	4.24	4.52	2.50	0.21	99.86
0.549	61.06	0.47	11.44	10.10	0.09	5.16	4.28	4.57	2.41	0.26	99.84
0.555	60.35	0.47	11.48	10.48	0.10	5.39	4.46	4.67	2.28	0.21	99.88
0.573	60.77	0.43	11.63	10.28	0.13	5.38	4.46	4.22	2.31	0.28	99.89
0.581	59.34	0.45	11.41	11.00	0.15	5.85	4.66	4.57	2.23	0.20	99.86
0.600	59.37	0.56	11.44	10.89	0.10	5.86	4.71	4.63	2.07	0.25	99.87
0.613	59.19	0.41	11.23	10.92	0.13	5.95	4.93	4.65	2.10	0.36	99.87
0.639	58.74	0.49	11.19	11.19	0.18	6.28	4.87	4.49	2.08	0.35	99.87
0.659	58.33	0.47	11.21	11.57	0.14	6.42	5.17	4.30	2.01	0.30	99.92
0.687	57.80	0.42	11.18	11.67	0.13	6.73	5.20	4.52	1.78	0.43	99.85
0.712	56.40	0.44	11.26	12.24	0.19	7.14	5.67	4.35	1.80	0.44	99.92
0.737	55.77	0.43	11.13	12.87	0.20	7.31	5.93	4.15	1.68	0.45	99.91
0.760	55.26	0.44	11.10	13.13	0.10	7.54	6.07	4.13	1.60	0.52	99.90
0.782	54.60	0.50	11.26	13.41	0.13	7.89	6.20	4.03	1.42	0.44	99.89
0.795	53.78	0.48	11.10	13.88	0.16	8.17	6.33	4.00	1.46	0.49	99.84
0.827	53.65	0.53	11.13	13.93	0.13	8.20	6.45	3.88	1.41	0.61	99.91
0.837	52.07	0.53	10.99	14.43	0.18	9.03	6.65	4.27	1.27	0.55	99.95
0.852	51.91	0.47	10.87	14.74	0.15	9.05	6.72	4.21	1.30	0.51	99.94
0.864	52.70	0.52	11.18	14.75	0.19	8.63	6.59	3.64	1.18	0.55	99.93
0.882	51.82	0.56	11.14	15.12	0.20	8.92	6.72	3.66	1.22	0.57	99.93
0.897	51.29	0.55	10.96	15.07	0.11	9.25	6.92	3.92	1.23	0.64	99.95
0.898	51.74	0.59	10.82	14.94	0.16	9.21	7.07	3.75	1.08	0.60	99.95
0.918	51.65	0.55	10.89	15.42	0.19	9.02	7.05	3.54	1.12	0.50	99.94
0.925	50.21	0.57	11.12	15.60	0.10	9.57	7.44	3.54	0.99	0.80	99.94
0.933	50.63	0.57	10.95	15.73	0.22	9.57	7.22	3.49	0.97	0.57	99.92
0.952	50.84	0.51	11.06	15.47	0.12	9.31	7.15	3.69	1.10	0.70	99.96
0.953	49.97	0.54	11.15	16.07	0.10	9.87	7.24	3.39	0.91	0.70	99.95
0.958	50.57	0.57	11.00	15.79	0.14	9.62	7.39	3.46	0.89	0.48	99.92
0.964	49.88	0.57	10.92	15.99	0.09	9.83	7.81	3.38	0.82	0.66	99.96
0.970	49.78	0.59	10.87	16.02	0.14	10.09	7.59	3.26	0.93	0.71	99.96
0.982	49.39	0.54	10.87	16.57	0.12	10.08	7.79	3.24	0.73	0.67	99.99
1.000	49.25	0.56	10.72	16.78	0.13	10.16	7.81	3.11	0.80	0.65	99.97

respect to the spectra of the two end-members as a function of the Raman parameter R_p using the following equation:

$$I_n = E_B \cdot R_p + E_R \cdot (1 - R_p) \quad (1)$$

where I_n represents the normalized intensity for each wave number of the acquired Raman spectra and E_B and E_R represent the normalized intensities of the same wave number for the basalt end-member and rhyolite end-member Raman spectra, respectively.

The obtained Raman parameters using the equation (1), associated to each spectrum, are reported in Table 1 and plotted in Figure 4 as a function of chemical composition.

Note that the R_p parameter is equal to 0 at the rhyolitic end-member (distance 845 μm) and equal to 1 at the basaltic end-member.

The Raman parameter (R_p) functions as a proxy to track the change of the spectra with respect to the two iron-rich end-member compositions (i.e., basaltic and rhyolitic). In this manner, the R_p can be used as a tool to approximate the chemical composition of silicate glasses constrained to this specific chemical interval.

In order to retrieve the chemical composition, each major element was parameterized using the following second degree polynomial equation:

$$y = a \cdot R_p^2 + b \cdot R_p + c \quad (2)$$

where y represents the calculated concentration in wt % oxide (SiO₂, Al₂O₃, FeO, CaO, MgO, Na₂O, and K₂O) and a , b , and c are the fit parameters (Table 2). In addition, in Table S2 the fit parameters necessary to calculate the chemical composition expressed in mol% are reported. Due to the low absolute concentration

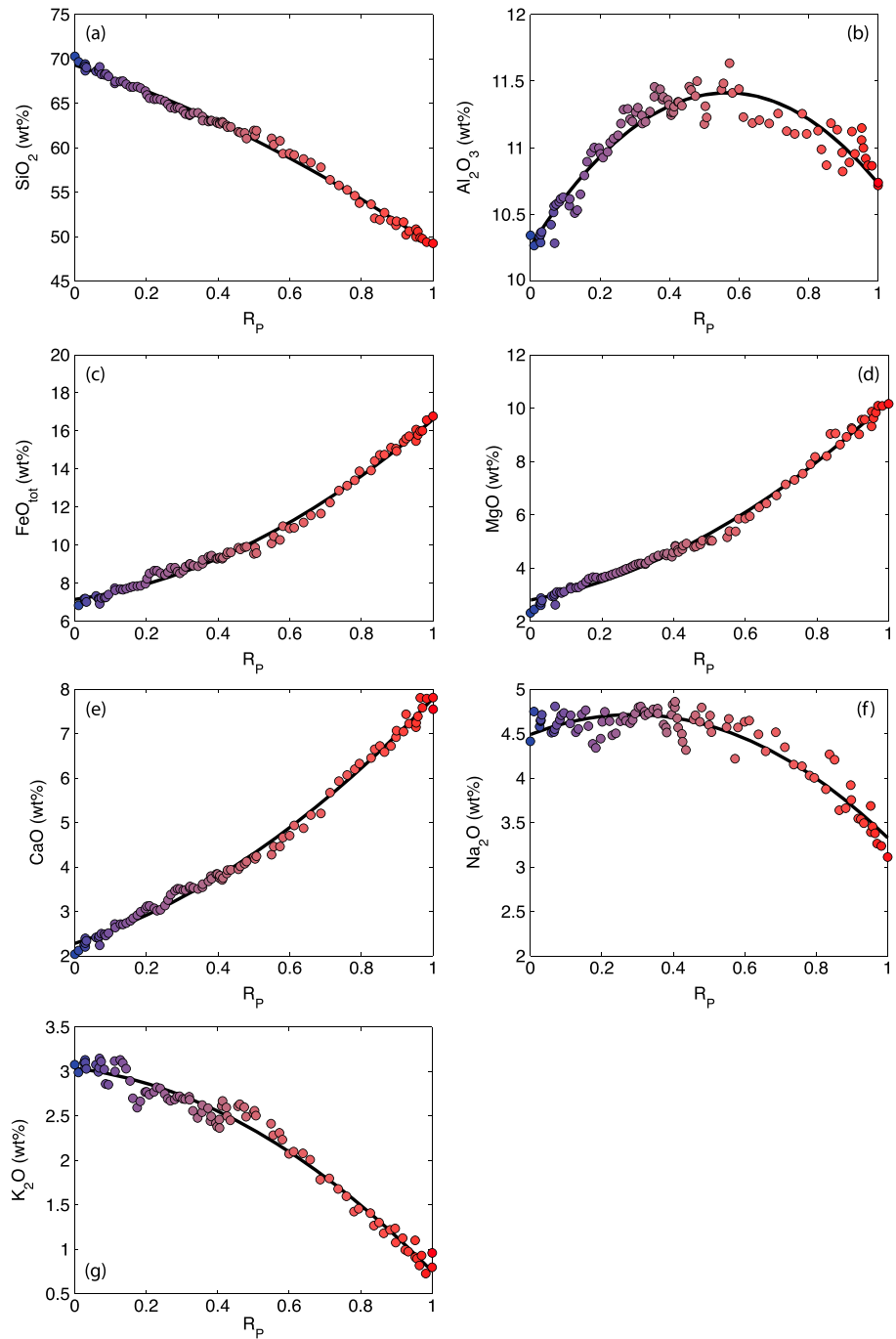


Figure 4. Glass chemistry as a function of Raman parameter (R_p ; using equation (1)). The parameterizations obtained using equation (2) are reported as solid lines. Fit parameters are listed in Table 2.

of TiO_2 and MnO in all samples, and in consequence of the related scatter due to analytical uncertainty in the EMPA analysis, the goodness of fit for both these elements (R^2 values of 0.6866 and 0.0565, respectively) is poor. Therefore, by the use of equation (2), with the calculated R_p (Table 1), the sample chemical composition can be calculated using the collected Raman spectra. In Figure 5 we report a comparison between the estimated versus measured chemical compositions of the analyzed samples.

Matlab© and Excel© files of the Raman model are provided in Data Sets S1 and S2 in the supporting information together with a brief description provided in Text S1 in the supporting information.

Table 2. Fitting Parameters of the Quadratic Equation ($y = a R_p^2 + b R_p + c$) Used to Parameterize the Chemical Composition (y , in wt %) as a Function of Raman Parameters (R_p)^a

Oxide	a	b	c	R^2
SiO ₂	-7.05 ± 0.63	-13.22 ± 0.65	69.30 ± 0.13	0.994
TiO ₂	0.23 ± 0.05	-0.06 ± 0.05	0.41 ± 0.01	0.687
Al ₂ O ₃	-3.60 ± 0.15	4.07 ± 0.15	10.26 ± 0.03	0.893
FeO	6.77 ± 0.35	2.69 ± 0.36	7.16 ± 0.07	0.992
MnO	-0.01 ± 0.04	0.03 ± 0.04	0.12 ± 0.01	0.057
MgO	5.00 ± 0.26	2.49 ± 0.27	2.80 ± 0.06	0.992
CaO	2.92 ± 0.17	2.59 ± 0.17	2.28 ± 0.04	0.994
Na ₂ O	-2.72 ± 0.19	1.56 ± 0.19	4.49 ± 0.04	0.890
K ₂ O	-1.80 ± 0.14	-0.49 ± 0.15	3.04 ± 0.03	0.976
P ₂ O ₅	0.51 ± 0.06	0.17 ± 0.06	0.02 ± 0.01	0.950

^aThe goodness of fit is indicated by the correlation coefficient (R^2).

4.2. Model Validation

Our approach has been validated using four samples for which the chemical composition was independently measured. As reported above, Martian basalts are considerably enriched in iron respect to terrestrial ones which exhibit an average of FeO_{tot} abundance of ~12 wt % [Chevrel *et al.*, 2014]. Because of this, we decided to first test our model using Mars analogue glasses [Chevrel *et al.*, 2014].

In order to do so, we acquired the Raman spectrum (Figure S2) of a reduced Fe-rich synthetic basaltic glass (AdMB-S6, Fe²⁺/Fe_{tot} = 0.63) with a chemical composition (Table 3) corresponding to the Adirondack class rock (Gusev plains on Mars [Ming *et al.*, 2008]).

Combining the acquired Raman spectrum with the spectra of the end-members we obtained a Raman parameter $R_p = 0.97$ (Table 3) close to a basaltic composition (Table 1). Moreover, using the equation (2) we were able to approximate the chemical composition of the AdMB-S6 sample (Table 3).

In particular, the estimated SiO₂ and Al₂O₃ contents are 49.96 and 10.84 wt %, respectively (Table 3), while the measured values are 47.62 and 11.13 wt %, respectively. Our model slightly underestimates the measured FeO content (16.08 versus 18.95 wt %). The reason for this mismatch is, as outlined above, that this sample has a certain different chemical composition, being slightly lower in silica and more significantly higher in

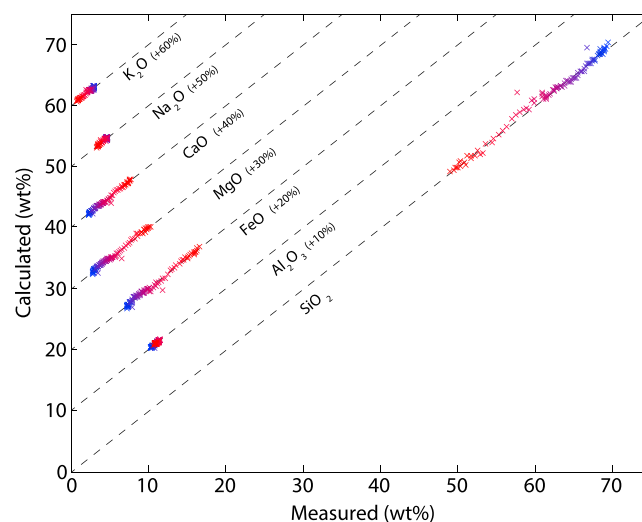


Figure 5. Measured oxide compositions compared to compositions calculated with equation (2). The dashed lines represent 1:1 relationships. To improve result visualization, calculated contents of Al₂O₃, FeO, MgO, CaO, Na₂O, and K₂O were shifted of 10, 20, 30, 40, 50, and 60 wt %, respectively. Symbol color scale codifies the evolution of chemical composition of the investigated glasses (see Figure 1).

iron content with respect to our basaltic end-member. The presence of iron may strongly affect the vibrational features in the Raman spectrum. In fact, as a result of this difference in iron content, the AdMB-S6 sample exhibits a lower, normalized intensity in the LW region with respect to the basaltic end-member. The (main) peak intensity at $\sim 965 \text{ cm}^{-1}$ may be used to investigate in more detail the effect of iron on the Raman spectra [Di Genova *et al.*, 2016, and references therein]. The estimated alkali content (Na₂O = 3.46 wt %, K₂O = 0.89 wt %) is slightly higher than the measured one (Na₂O = 2.84 wt %, K₂O = 0.17 wt %), while the alkaline earth content (CaO = 8.53 wt % and MgO = 9.13 wt %) is adequately predicted (7.52 and 9.88 wt %, respectively).

Table 3. Measured and Calculated Chemistry of Analyzed External Samples Used to Test the Proposed Raman Model

Oxide (wt %)	AdMB-S6		IAMB-S5		MSA		MSB	
	Measured	Calculated ^a	Measured	Calculated ^a	Measured	Calculated ^a	Measured	Calculated ^a
SiO ₂	47.62	49.96 ± 1.36	53.53	52.50 ± 1.18	59.58	60.99 ± 0.61	55.18	57.12 ± 0.86
TiO ₂	0.64	0.56 ± 0.1	1.04	0.53 ± 0.09	0.58	0.43 ± 0.05	0.72	0.47 ± 0.06
Al ₂ O ₃	11.13	10.84 ± 0.31	9.26	11.09 ± 0.27	17.94	11.41 ± 0.14	18.50	11.38 ± 0.2
FeO	18.95	16.08 ± 0.74	16.56	14.63 ± 0.64	6.28	10.22 ± 0.33	8.20	12.12 ± 0.47
MnO	0.43	0.15 ± 0.09	0.34	0.14 ± 0.08	0.20	0.14 ± 0.04	0.21	0.14 ± 0.06
MgO	9.13	9.88 ± 0.57	8.20	8.76 ± 0.49	2.86	5.31 ± 0.26	3.45	6.81 ± 0.36
CaO	8.53	7.52 ± 0.36	5.81	6.75 ± 0.31	7.71	4.32 ± 0.16	9.16	5.40 ± 0.23
Na ₂ O	2.84	3.46 ± 0.4	3.77	3.79 ± 0.35	3.75	4.60 ± 0.18	3.49	4.30 ± 0.25
K ₂ O	0.17	0.89 ± 0.3	0.78	1.25 ± 0.26	0.84	2.34 ± 0.14	0.61	1.88 ± 0.19
P ₂ O ₅	0.57	0.67 ± 0.13	0.71	0.56 ± 0.12	-	0.24 ± 0.06	-	0.38 ± 0.08
tot.	100.00	100.00	100.00	100.00	99.74	100.00	99.52	100.00
R _p ^b		0.97		0.87		0.50		0.68

^aUsing equation (2).

^bCalculated Raman parameter using equation (1).

A further synthetic glass (IAMB-S5 from *Chevrel et al.* [2014], $Fe^{2+}/Fe_{tot} = 0.88$) was selected for Raman measurement and chemical estimation. The chemical composition of this sample corresponds to the Irvine class rock that is an alkali basalt found at the Columbia Hills inside the Gusev crater on Mars [*Ming et al.*, 2008]. The IAMB-S5 is characterized by a more evolved and more alkali-rich composition than the AdMB-S6 sample. Interestingly, the calculated Raman parameter is 0.87, which confirms the higher degree of polymerization of this sample than AdMB-S6. Indeed, the measured SiO₂ content is 53.53 wt % (Table 3), while the calculated is 52.50 wt %.

In addition to the iron-rich synthetic basaltic glasses, we also used terrestrial glasses in order to validate our model for silica-rich compositions. For this purpose, we collected the Raman spectrum of a basaltic-andesite glass (MSB, Figure S2), and in addition, we used the andesitic Raman spectrum reported in *Di Genova et al.* [2015] (MSA, Figure S2). The chemical compositions (EPMA) are reported in Table 3 together with the model prediction.

For both samples the silica content was well predicted; the estimated MSB SiO₂ content is 57.12 wt %, while the measured content is 55.18 wt %; for the MSA sample the estimation is 60.99 wt %, while the measured value is 59.58 wt %. As expected, the model overestimates the FeO content of both samples (Table 3) as calc-alkaline glasses are significantly less iron rich compared to the glasses employed to develop our model (12.12 versus 8.20 wt % for MSB and 10.22 versus 6.28 wt % for MSA). Interestingly, as a result of the iron overestimation, the Al₂O₃ content is similarly underestimated (11.38 versus 18.50 wt % for MSB; 11.41 versus 17.94 wt % for MSA). The total amount of alkali and alkaline earth cations is adequately approximated (Table 3).

4.3. Implications for Mars

Our understanding of Mars has seen significant improvements in recent years owing to the study of meteorites (see *McSween and McLennan* [2013] for a data compilation) and development of orbiters and rovers (see *McSween* [2015] for a review). This has led to a considerable advancement in high-resolution topographic maps [*Bibring et al.*, 2006] as well as understanding of the composition and physical processes associated to the Martian surface [e.g., *Squyres et al.*, 2012; *Stolper et al.*, 2013; *Sautter et al.*, 2015]. In particular, the rovers that perform in situ analyses on Martian surface are a unique source of data. Although the instruments carried by rovers are able to obtain precise bulk rock composition and mineral characteristics [*McSween*, 2015], the amorphous phase compositions that are so valuable for estimating processes of formation crucial to understand Martian surface conditions are still absent.

The growing development of Raman spectrometers as powerful technique for the in situ and remotely controlled rapid identification of organic and inorganic amorphous materials is therefore particularly relevant for future mission to Mars. In this respect, the European Space Agency and the National Aeronautics and Space Administration are currently testing and enhancing rovers equipped with Raman spectrometers for the ExoMars and Mars 2020 missions.

Considering the abundance of glassy material found on Mars, either as sedimentary deposits, volcanic products, or impact-related deposits [Horgan and Bell, 2012; Minitti et al., 2013; Cannon and Mustard, 2015], we need to be able to interpret all Raman spectral signatures in order to characterize any potential glassy phase and study the processes of its formation.

Our calibration for Raman spectra can be directly applied to interpret future analyses from forthcoming Mars missions. This fundamental information would resolve several issues, e.g., (1) detailing the processes involved in volcanic events and especially the cooling processes [e.g., Dingwell, 1996], (2) determine the origin of the widespread area of glassy sand observed by Horgan and Bell [2012], (3) yield new information in respect to the presence of water and therefore the potential for hosting life and (4) characterize glassy spherules and impactites that could host traces of life [Cannon and Mustard, 2015].

5. Conclusions

Based on the results and discussion presented above we draw the following conclusions:

1. Raman spectra can be used to determine the chemical composition of glasses of a compositional range expected to be encountered on Mars.
2. The presented data help to expand the database of Raman spectra and corresponding chemical analysis reported by Di Genova et al. [2015, 2016] and highlight the need for continued development of this database to broaden its applicability in Earth Science as well as for extraterrestrial missions to Mars and other planets.
3. The model for estimation of the chemical composition of silicate glasses will expand the working range of the Raman spectrometers mounted on both ExoMars and MARS 2020 to include in situ analysis of the chemical composition and water content of silicate glasses.
4. Characterization of glassy material encountered on Mars surface will help to constrain the geological processes acting on the Martian surface.

Acknowledgments

This research was funded by the ERC Advanced Grant 247076 – EVOKES. We acknowledge D. Mueller for EPMA analysis. The authors are grateful to S.A. Hauck II and two anonymous reviewers for very helpful comments, which have helped to improve the paper. The first author thanks A.L. Huber for useful discussion and encouraging support. S. Kolzenburg appreciates a Compagnia San Paolo PhD fellowship. A. Vona acknowledges the financial support by Italian MIUR project PRIN 2010-11 (2010TT22SC_003). The data used are listed in the references, tables, and supporting information. Please contact the corresponding author for access to the raw Raman spectra that this study is based upon.

References

- Baratoux, D., M. J. Toplis, M. Monnereau, and O. Gasnault (2011), Thermal history of Mars inferred from orbital geochemistry of volcanic provinces, *Nature*, *472*(7343), 338–341, doi:10.1038/nature10220.
- Bathgate, E. J., H. E. Maynard-Casely, G. Caprarelli, L. Xiao, B. Stuart, K. T. Smith, and R. Pogson (2015), Raman, FTIR and XRD study of Icelandic tephra minerals: Implications for Mars, *J. Raman Spectrosc.*, *46*(10), 846–855, doi:10.1002/jrs.4694.
- Behrens, H., J. Roux, D. R. Neuville, and M. Siemann (2006), Quantification of dissolved H₂O in silicate glasses using confocal microRaman spectroscopy, *Chem. Geol.*, *229*(1–3), 96–112, doi:10.1016/j.chemgeo.2006.01.014.
- Bell, R. J., and P. Dean (1972), The structure of vitreous silica: Validity of the random network theory, *Philos. Mag.*, *25*(6), 1381–1398, doi:10.1080/14786437208223861.
- Bell, R. J., N. F. Bird, and P. Dean (1968), The vibrational spectra of vitreous silica, germania and beryllium fluoride, *J. Phys. C Solid State Phys.*, *1*(2), 299–303, doi:10.1088/0022-3719/1/2/304.
- Bibring, J.-P., et al. (2006), Global mineralogical and aqueous Mars history derived from OMEGA/Mars Express data, *Science*, *312*(5772), 400–404.
- Bish, D. L., et al. (2013), X-ray diffraction results from Mars Science Laboratory: Mineralogy of Rocknest at Gale crater, *Science*, *341*, 1238932, doi:10.1126/science.1238932.
- Blake, D. F., et al. (2013), Curiosity at Gale crater, Mars: Characterization and analysis of the Rocknest sand shadow, *Science*, *341*(6153), 1,239,505, doi:10.1126/science.1239505.
- Cannon, K. M., and J. F. Mustard (2015), Preserved glass-rich impactite on Mars, *Geology*, *43*(7), 635–638, doi:10.1130/G36953.1.
- Chakraborty, S., D. B. Dingwell, and D. C. Rubie (1995), Multicomponent diffusion in ternary silicate melts in the system K₂O-Al₂O₃-SiO₂: II. Mechanisms, systematics, and geological applications, *Geochim. Cosmochim. Acta*, *59*(2), 265–277.
- Chevrel, M. O., D. Baratoux, K. U. Hess, and D. B. Dingwell (2014), Viscous flow behavior of tholeiitic and alkaline Fe-rich Martian basalts, *Geochim. Cosmochim. Acta*, *124*, 348–365, doi:10.1016/j.gca.2013.08.026.
- Christensen, P. R., et al. (2005), Evidence for magmatic evolution and diversity on Mars from infrared observations, *Nature*, *436*, 504–509, doi:10.1038/nature03639.
- Dingwell, D. B. (1996), Volcanic dilemma: Flow or blow?, *Science*, *273*(5278), 1054–105.
- Downs, R. T. (2015), Determining mineralogy on Mars with the CheMin X-ray diffractometer, *Electron. J. Severe Storms Meteorol.*, *11*(1), 45–50, doi:10.2113/gselements.11.1.45.
- Dreibus, G., and H. Wanke (1984), Accretion of the Earth and the inner planets, in *Proceedings of the 27th International Geological Congress*, pp. 1–20, Moscow.
- Furukawa, T., K. E. Fox, and W. B. White (1981), Raman spectroscopic investigation of the structure of silicate glasses. III. Raman intensities and structural units in sodium silicate glasses, *J. Chem. Phys.*, *75*(7), 3226, doi:10.1063/1.442472.
- Di Genova, D., C. Romano, K. U. Hess, A. Vona, B. T. Poe, D. Giordano, D. B. Dingwell, and H. Behrens (2013), The rheology of peralkaline rhyolites from Pantelleria Island, *J. Volcanol. Geotherm. Res.*, *249*(1), 201–216.
- Di Genova, D., D. Morgavi, K. U. Hess, D. R. Neuville, N. Borovkov, D. Perugini, and D. B. Dingwell (2015), Approximate chemical analysis of volcanic glasses using Raman spectroscopy, *J. Raman Spectrosc.*, *46*(12), 1235–1244, doi:10.1002/jrs.4751.
- Di Genova, D., K.-U. Hess, M. O. Chevrel, and D. B. Dingwell (2016), Models for the estimation of Fe³⁺/Fe_{tot} ratio in terrestrial and extraterrestrial alkali- and iron-rich silicate glasses using Raman spectroscopy, *Am. Mineral.*, 1–37, doi:10.2138/am-2016-5534CCBYNCND.

- Ghosal, S., R. O. Sack, M. S. Ghiorso, and M. E. Lipschutz (1998), Evidence for a reduced, Fe-depleted Martian mantle source region of shergottites, *Contrib. Mineral. Petrol.*, *130*(3–4), 346–357, doi:10.1007/s004100050370.
- Greenberger, R. N., J. F. Mustard, B. L. Ehlmann, D. L. Blaney, E. A. Cloutis, J. H. Wilson, R. O. Green, and A. A. Fraeman (2015), Imaging spectroscopy of geological samples and outcrops: Novel insights from microns to meters, *GSA Today*, *25*(12), 4–10, doi:10.1130/GSATG252A.1.
- Grotzinger, J. P., J. A. Crisp, and A. R. Vasavada (2015), Curiosity's mission of exploration at Gale Crater, Mars, *Electron. J. Severe Storms Meteorol.*, *11*(1), 19–26, doi:10.2113/gselements.11.1.19.
- Herd, C. D. K., L. E. Borg, J. H. Jones, and J. J. Papike (2002), Oxygen fugacity and geochemical variations in the Martian basalts: Implications for Martian basalt petrogenesis and the oxidation state of the upper mantle of Mars, *Geochim. Cosmochim. Acta*, *66*(11), 2025–2036, doi:10.1016/S0016-7037(02)00828-1.
- Horgan, B., and J. F. Bell (2012), Widespread weathered glass on the surface of Mars, *Geology*, *40*, 391, doi:10.1130/G32755.1.
- Hutchinson, I. B., R. Ingle, G. M. Howell, L. Harris, M. Mchugh, C. Malherbe, and J. Parnell (2014), Raman spectroscopy on Mars: Identification of geological and bio-geological signatures in Martian analogues using miniaturized Raman spectrometers, *Philos. Trans. R. Soc. Lond.*, *372*.
- Kah, L. C. (2015), Images from Curiosity: A New Look at Mars, *Electron. J. Severe Storms Meteorol.*, *11*(1), 27–32, doi:10.2113/gselements.11.1.27.
- Lange, R. A., and I. S. E. Carmichael (1990), Thermodynamic properties of silicate liquids with emphasis on density, thermal expansion and compressibility, *Rev. Mineral. Geochem.*, *24*(1), 25–64.
- Long, D. A. (1977), *Raman Spectroscopy*, pp. 276, McGraw-Hill, New York, 2(600).
- Le Losq, C., D. R. Neuville, R. Moretti, and J. Roux (2012), Determination of water content in silicate glasses using Raman spectrometry: Implications for the study of explosive volcanism, *Am. Mineral.*, *97*(5–6), 779–790, doi:10.2138/am.2012.3831.
- McMillan, P. F. (1984), A Raman spectroscopic study of glasses in the system CaO-MgO-SiO₂, *Am. Mineral.*, *69*, 645–659.
- McMillan, P. F., B. Piriou, and A. Navrotsky (1982), A Raman spectroscopic study of glasses along the joins silica-calcium aluminate, silica-sodium aluminate, and silica-potassium aluminate, *Geochim. Cosmochim. Acta*, *46*(11), 2021–2037, doi:10.1016/0016-7037(82)90182-X.
- McMillan, P. F., B. T. Poe, P. H. Gillet, and B. Reynard (1994), A study of SiO₂ glass and supercooled liquid to 1950 K via high-temperature Raman spectroscopy, *Geochim. Cosmochim. Acta*, *58*(17), 3653–3664, doi:10.1016/0016-7037(94)90156-2.
- McSween, H. Y. (2015), Petrology on Mars, *Am. Mineral.*, *100*(11–12), 2380–2395, doi:10.2138/am-2015-5257.
- McSween, H. Y., and S. M. McLennan (2013), Mars, in *Treatise on Geochemistry*, 2nd ed., pp. 251–300, Elsevier, Oxford.
- McSween, H. Y., D. D. Eisenhour, L. A. Taylor, M. Wadhwa, and G. Crozaz (1996), QUE94201 shergottite: Crystallization of a Martian basaltic magma, *Geochim. Cosmochim. Acta*, *60*(22), 4563–4569, doi:10.1016/S0016-7037(96)00265-7.
- Ming, D. W., et al. (2008), Geochemical properties of rocks and soils in Gusev crater, Mars: Results of the Alpha Particle X-Ray Spectrometer from Cumberland Ridge to Home Plate, *J. Geophys. Res. E: Planets*, *113*(12), doi:10.1029/2008JE003195.
- Minitti, M. E., et al. (2013), MAHLI at the Rocknest sand shadow: Science and science-enabling activities, *J. Geophys. Res. Planets*, *118*, 2338–2360, doi:10.1002/2013JE004426.
- Motamedi, K., et al. (2015), Design of a Mars atmosphere simulation chamber and testing a Raman Laser Spectrometer (RLS) under conditions pertinent to Mars rover missions, *EPJ Tech. Instrum.*, *2*(1), 15, doi:10.1140/epjti/s40485-015-0025-7.
- Mustard, J. et al. (2013), Report of the Mars 2020 Science Definition Team, *Mars Explor. Progr. Anal. Gr.*, 155–205.
- Mysen, B. O. (1988), Relationships between simple synthetic and complex natural systems, pp. 70–71.
- Mysen, B. O., D. Virgo, and C. M. Scanfe (1980), Relations between the anionic structure and viscosity of silicate melts - A Raman spectroscopic study, *Am. Mineral.*, *65*, 690–710.
- Mysen, B. O., D. Virgo, and F. A. Seifert (1982), The structure of silicate melts: Implications for chemical and physical properties of natural magma, *Rev. Geophys.*, *20*(3), 353–383, doi:10.1029/RG020i003p00353.
- Neuville, D. R., and B. O. Mysen (1996), Role of aluminium in the silicate network: In situ, high-temperature of glasses and melts on the join SiO₂-NaAlO₂, *Geochim. Cosmochim. Acta*, *60*(96), 1727–1737.
- Neuville, D. R., D. de Ligny, and G. S. Henderson (2014), Advances in Raman spectroscopy applied to Earth and material sciences, *Rev. Mineral.*, *78*, 509–541.
- Newsom, H. E., et al. (2015), Gale crater and impact processes – Curiosity's first 364 Sols on Mars, *Icarus*, *249*, 108–128, doi:10.1016/j.icarus.2014.10.013.
- Prinsloo, L. C., P. Colombari, J. D. Brink, and I. Meiklejohn (2011), A Raman spectroscopic study of the igneous rocks on Marion Island: A possible terrestrial analogue for the geology on Mars, *J. Raman Spectrosc.*, *42*(4), 626–632, doi:10.1002/jrs.2756.
- Righter, K., H. Yang, G. Costin, and R. T. Downs (2008), Oxygen fugacity in the Martian mantle controlled by carbon: New constraints from the nakhlite MIL 03346, *Meteorit. Planet. Sci.*, *43*(10), 1709–1723, doi:10.1111/j.1945-5100.2008.tb00638.x.
- Rossano, S., and B. O. Mysen (2012), Chapter 9: Raman spectroscopy of silicate glasses and melts in geological systems, in *Applications of Raman Spectroscopy to Earth Sciences and Cultural Heritage, EMU Notes in Mineralogy*, vol. 12, European Mineralogical Union and the Mineralogical Society of Great Britain & Ireland, London.
- Sautter, V., M. J. Toplis, R. C. Wiens, A. Cousin, C. Fabre, O. Gasnault, S. Maurice, O. Forni, and J. Lasue (2015), In situ evidence for continental crust on early Mars, *Nat. Geosci.*, *1*, doi:10.1038/NGEO2474.
- Seifert, F., B. O. Mysen, and D. Virgo (1982), Three-dimensional network structure of quenched melts (glass) in the systems SiO₂-NaAlO₂, SiO₂-CaAl₂O₄ and SiO₂-MgAl₂O₄, *Am. Mineral.*, *67*(1981), 696–717.
- Shuker, R., and W. Cammon (1970), Raman-scattering selection-rule breaking and the density of states in amorphous materials, *Phys. Rev. Lett.*, *25*(4), 222–225.
- Squyres, S. W., et al. (2012), Ancient impact and aqueous processes at Endeavour Crater, Mars, *Science*, *336*(6081), 570–576, doi:10.1126/science.1220476.
- Stolper, E. M., et al. (2013), The petrochemistry of Jake_M: A Martian mugearite, *Science*, *341*(6153), 1239463, doi:10.1126/science.1239463.
- Tarcea, N., T. Frosch, P. Rösch, M. Hilchenbach, T. Stuffer, S. Hofer, H. Thiele, R. Hochleitner, and J. Popp (2008), Raman spectroscopy—A powerful tool for in situ planetary science, *Space Sci. Rev.*, *135*(1–4), 281–292, doi:10.1007/s11214-007-9279-y.
- Thomas, R. (2000), Determination of water contents of granite melt inclusions by confocal laser Raman microprobe spectroscopy, *Am. Mineral.*, *85*, 868–872.
- Vaniman, D. T., et al. (2013), Mineralogy of a mudstone at Yellowknife Bay, Gale crater, Mars, *Science*, *343*, 1243480, doi:10.1126/science.1243480.
- Zajacz, Z., et al. (2005), A composition-independent quantitative determination of the water content in silicate glasses and silicate melt inclusions by confocal Raman spectroscopy, *Contrib. Mineral. Petrol.*, *150*(6), 631–642, doi:10.1007/s00410-005-0040-9.